



instruments

CITESCORE
2.6

Article

Muography for Inspection of Civil Structures

Subhendu Das, Sridhar Tripathy, Priyanka Jagga, Purba Bhattacharya, Nayana Majumdar and Supratik Mukhopadhyay

Special Issue

Muography, Applications in Cosmic-Ray Muon Imaging

Edited by





Dr. Alan D. Bross and Dr. Jacques E. Marteau



<https://doi.org/10.3390/instruments6040077>

Article

Muography for Inspection of Civil Structures

Subhendu Das ^{1,2,*} , Sridhar Tripathy ³, Priyanka Jagga ^{1,t} , Purba Bhattacharya ⁴, Nayana Majumdar ^{1,2} 
and Supratik Mukhopadhyay ^{1,2} 

- ¹ Applied Nuclear Physics Division, Saha Institute of Nuclear Physics, Sector I, AF Block, Bidhannagar, Kolkata 700064, India
- ² Homi Bhabha National Institute, Training School Complex, Anushaktinagar, Mumbai 400094, India
- ³ Department of Physics, University of California, Davis, One Shields Avenue, Davis, CA 95616, USA
- ⁴ Department of Physics, School of Basic and Applied Sciences, Adamas University, Barbaria, Jagannathpur, North 24 Parganas, Kolkata 700126, India
- * Correspondence: subhendu.das@saha.ac.in
- † Project student.

Abstract: Aging infrastructure is a threatening issue throughout the world. Long exposure to oxygen and moisture causes premature corrosion of reinforced concrete structures leading to the collapse of the structures. As a consequence, real-time monitoring of civil structures for rust becomes critical in avoiding mishaps. Muon scattering tomography is a non-destructive, non-invasive technique which has shown impressive results in 3D imaging of civil structures. This paper explores the application of advanced machine learning techniques in identifying a rusted reinforced concrete rebar using muon scattering tomography. To achieve this, we have simulated the performance of an imaging prototype setup, designed to carry out muon scattering tomography, to precisely measure the rust percentage in a rusted rebar. We have produced a 2D image based on the projected 3D scattering vertices of the muons and used the scattering vertex density and average deviation angle per pixel as the distinguishing parameter for the analysis. A filtering algorithm, namely the Pattern Recognition Method, has been employed to eliminate background noise. Since this problem boils down to whether or not the material being analyzed is rust, i.e., a classification problem, we have adopted the well-known machine learning algorithm Support Vector Machine to identify rust in the rusted reinforced cement concrete structure. It was observed that the trained model could easily identify 30% of rust in the structure with a nominal exposure of 30 days within a small error range of 7.3%.

Keywords: machine learning; muon scattering tomography; non-destructive evaluation; Geant4; support vector machine; reinforced cement concrete



Citation: Das, S.; Tripathy, S.; Jagga, P.; Bhattacharya, P.; Majumdar, N.; Mukhopadhyay, S. Muography for Inspection of Civil Structures. *Instruments* **2022**, *6*, 77. <https://doi.org/10.3390/instruments6040077>

Academic Editors: Alan D. Bross and Jacques E. Marteau

Received: 30 September 2022

Accepted: 9 November 2022

Published: 18 November 2022

Publisher's Note: MDPI stays neutral with regard to jurisdictional claims in published maps and institutional affiliations.



Copyright: © 2022 by the authors. Licensee MDPI, Basel, Switzerland. This article is an open access article distributed under the terms and conditions of the Creative Commons Attribution (CC BY) license (<https://creativecommons.org/licenses/by/4.0/>).

1. Introduction

Reinforced Cement Concrete (RCC) structures have been the backbone of civil engineering for several decades. Reinforced concrete is an important building material in large-scale infrastructure: roads, bridges, tunnels, and buildings. Conventional concrete, despite having high compressive strength, lacks tensile strength which makes concrete brittle in face of shear and tension forces [1,2]. In the light of making concrete structures resistant to brittle and ductile mode failure, steel is added to the plain concrete. Steel due to its versatile properties can withstand these forces and, thus, is a perfect reinforcement for concrete [3]. It is however liable to damage due to corrosion, carbonation and chloride ingress. In order to avoid structural collapse, non-destructive testing methods are necessary to assess the quality of RCC structures. Additionally, knowledge of the type of defect and its precise location also improves the chances of averting the calamity. There are multiple Non-Destructive Evaluation (NDE) techniques that are typically used for imaging. These are ultrasonic tomography [4], infrared tomography [5,6], Ground Penetrating

Radar (GPR) [7], impact-echo [8]. These methods, however, have some limitations, which include the need for a high amount of heat for imaging non-conducting materials (active thermography), interference from environmental parameters, such as sunlight intensity (passive thermography), shadows of other bodies, wind, etc. Alternatively, radiological imaging methods (radiography) using X-rays and gamma-rays are very effective, but are not preferred due to their potential for biological hazards. Cosmic ray muon tomography is thus gaining traction for the imaging and monitoring of RCC structures.

Since the beginning of 1950s, cosmic ray muons have found applications in tomographic studies of large civil structures owing to their highly penetrative and less-interactive nature [9–13]. Other than imaging structures based on the differential flux of absorbed and penetrated muons, multiple scattering suffered by the muons while passing through matter due to their interaction with atomic nuclei, has also been exploited to scan targets, the underlying physics of which is formulated based on their atomic number, weight, and density [14–16]. This innovative NDE technique has found applications in scanning nuclear-waste containers, possibly-smuggled special nuclear materials in cargo containers, monitoring gate valve conditions, pipe wall thickness [17–20], etc. In addition to these, monitoring and imaging defects in large concrete structures have also emerged to be a substantial utilization of muon imaging [14,16,21].

This article showcases MST [22] as an NDE technique to image RCC structure and puts forward a recipe to discriminate rusted portions of steel rebars using the Geant4 simulation toolkit [23]. Subsequently, a classification-based Machine Learning (ML) algorithm has been employed to enhance image reconstruction and improve rust identification among targets involving similar material densities (steel (7.87 g/cc), rust (5.25 g/cc), and concrete (2.3 g/cc)). For training and validation, the ML model has been applied to a scenario with four blocks of materials: aluminium ($Z = 13$), iron ($Z = 26$), lead ($Z = 82$), and uranium ($Z = 92$) to address different ranges of atomic number and density. The scattering positions and corresponding angles of the muons as they pass through the blocks have been obtained from reconstruction of muon tracks from the muon hits as recorded by the muon trackers in the MST setup. This work has been accomplished by the Geant4 simulation. Based on these parameters, radiographic image production has been carried out. Next, by employing a Pattern Recognition Method (PRM) [24], the materials in focus have been separated from the background (air). The ML technique, mentioned above is a Support Vector Machine (SVM) [25] classifier which has been used to detect rust on a rebar in a RCC unit.

The working principle of MST has been detailed in Section 2 and the simulation model of the system has been described in Section 3. Discussion on image reconstruction of the target can be found in Section 4, followed by its analysis in Section 5. Finally, training the ML model on four blocks: Al, Fe, Pb, and U, and its implementation to segregate rust from the steel rebar have been reported in Section 6 along with its detailed analysis.

2. Principle of MST

Cosmic muons are high-energy (mean ≈ 4 GeV/c) particles with a relatively long lifetime ($2.2 \mu\text{s}$) and $\pm e$ charge. They are produced naturally in the atmosphere and have a flux rate of about 1 per cm^2/min at the sea level. Due to their greater mass ($105.66 \text{ MeV}/c^2$) [26], they can penetrate through large amount of materials without suffering any significant loss of energy. In addition to inelastic collisions with atomic electrons, muons passing through matter also suffer repeated elastic coulomb scattering from atomic nuclei. These collisions are individually governed by Rutherford's formula. The vast majority of these collisions result in a small angular deflection of the particle. The cumulative effect of these small angle scatterings compounds to a net deflection of the muon from its original trajectory. According to Moliere theory [27], the scattering angles projected on a plane obey the Gaussian distribution [22,28] and the standard deviation σ of the distribution is given by:

$$\sigma = \frac{13.6[\text{MeV}]}{\beta c p} \sqrt{L/X_0} (1 + 0.038 \ln(L/X_0)), \quad (1)$$

where p is the momentum of the muon, L is the distance traversed by it in the object, and β is the ratio of its velocity to the velocity of light. The radiation length, X_0 [cm], is a property of the object material which is given by:

$$X_0 = \frac{A \cdot 716.4 [\text{g}/\text{cm}^2]}{\rho \cdot Z(Z+1) \ln(287/\sqrt{Z})}, \quad (2)$$

where A , Z , and ρ are the atomic weight, number, and density of the material, respectively. Since the speed of muons is very close to the speed of light, the value of β can be approximated to 1. The value of $0.038 \ln(L/X_0)$ in Equation (1) is usually far less than 1. Thus, Equation (1) can be simplified to:

$$\sigma = \frac{13.6}{p} \sqrt{\frac{L}{X_0}} \quad (3)$$

In MST, the deviation angle plays a key role in differentiating materials as it relies on the atomic number, mass number, density, thickness of the material, and momentum of muons.

3. Geant4 Simulation Setup for MST

The concerned MST setup consists of six layers of position-sensitive gaseous ionization detectors that have been stacked parallelly, three each on either sides of the Region of Interest (RoI) subject to imaging with dimensions $80 \text{ cm} \times 80 \text{ cm} \times 40 \text{ cm}$. Four cubes of Al, Fe, Pb, and U with dimensions $10 \text{ cm} \times 10 \text{ cm} \times 10 \text{ cm}$ have been placed in the central plane of the RoI. The gaseous detectors used in the setup have dimensions $140 \text{ cm} \times 140 \text{ cm} \times 0.2 \text{ cm}$. Detectors with larger active areas have been chosen to maintain uniform muon hits across the lateral span of the RoI. The design parameters of the MST setup have followed from a preceding uniformity study that was carried out in [24]. The detectors have been assumed to have a 100% detection efficiency and a spatial resolution of $200 \mu\text{m}$, which has been added as a Gaussian uncertainty to the muon hits obtained from the simulation. Figure 1 shows the schematic representation of the model setup that has been subject to a muon flux to simulate the multiple Coulomb scattering of muons in the RoI. The Cosmic-Ray Shower Library (CRY) [29] has been used to produce muon flux for the latitude (22.57°) and altitude (sea-level) of the experimental laboratory. The FTFP_BERT physics list has been implemented to account for all the electromagnetic processes, weak interactions of charged particles and gamma radiations.

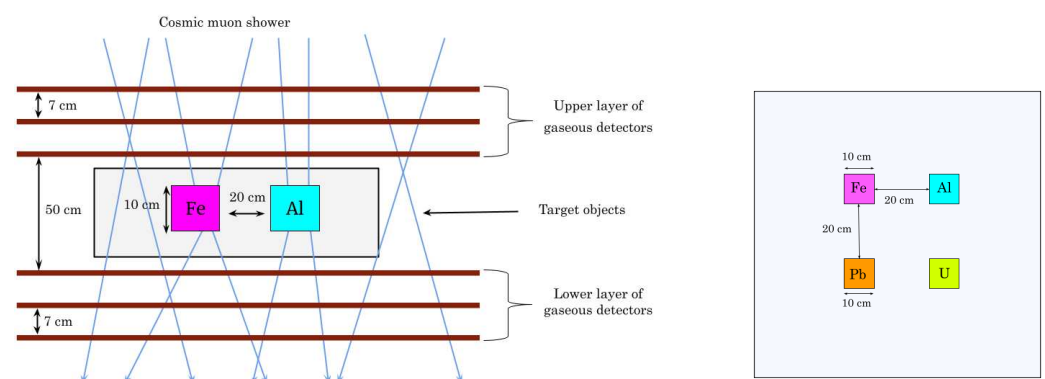


Figure 1. XZ projection (left) and XY projection (right) of simulation setup.

4. Track Reconstruction and Image Production

The incoming and outgoing muon hits on the detectors have been used for track reconstruction. The projection of the track on two orthogonal planes XZ and YZ have been used for determining two sets of least square fitting parameters for X and Y coordinates.

Since some of the hits produce statistical noise due to the applied resolution of the detector, several selection criteria have been implemented to choose only the relevant scatter points to reconstruct the tracks:

- The muon track must pass through all the detectors.
- The scattering location must fall inside the ROI.
- Angle between the track-lets constructed from any two pair of detectors in the upper/lower set, must not exceed 10 mrad.

4.1. Point of Closest Approach (PoCA) and Estimation of Angle of Deviation

The scattering events for which muon tracks satisfy the selection criteria, have been marked valid. To determine the probable 3D location of scattering vertex, the PoCA algorithm has been used. It is a well-established geometrical algorithm devised by L. Schultz et al. [17] which assumes that the scattering occurs due to a single scattering event in space at a single point. The scattering point obtains its coordinates by extrapolating the incident and scattered muon tracks by minimising the distance between the two tracks. A schematic of the algorithm is shown in Figure 2.

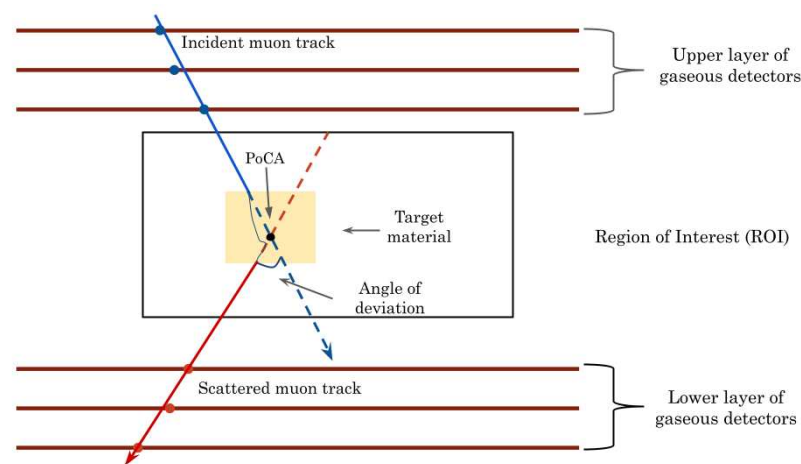


Figure 2. The incident muon hits have been marked by blue circles, and the incident track by solid blue line. The dotted blue line represents the extended incoming muon track vector. The muon hits on the lower set of detectors have been marked using red circles and the outgoing track using a solid red line. The extended outgoing track vector is marked using dotted red line. The PoCA reconstructed point has been marked using a black circle.

Using PoCA, we have obtained the scattering vertex and estimated the deviation angle for each muon event from the tracks. The events with deviation angle less than 10 mrad have not been considered in the analysis.

4.2. 2D Image Production

The scattering vertices obtained have been projected on the XY plane to obtain the 2D image or scattering map (S-map) of the target objects. In the case of 2D imaging, it is difficult to distinguish objects with different heights as the information along Z-direction is lost [24]. To address this, in the present work all the test objects have been considered to be of same dimension in all the directions. Thus, for the sake of simplicity we have projected the vertices on only the XY plane. The projected plane has been segmented into 80×80 pixels, each having an area of $1 \times 1 \text{ cm}^2$. The area of the pixels has been decided based on computation time, required accuracy in shape identification, and amount of data available. The S-map by projecting the scattering vertices in each pixel has been shown in the Figure 3. Important parameters, namely, scattering vertex density (ρ_c) and average deviation angle (θ_{avg}), have been calculated for each pixel for further analysis.

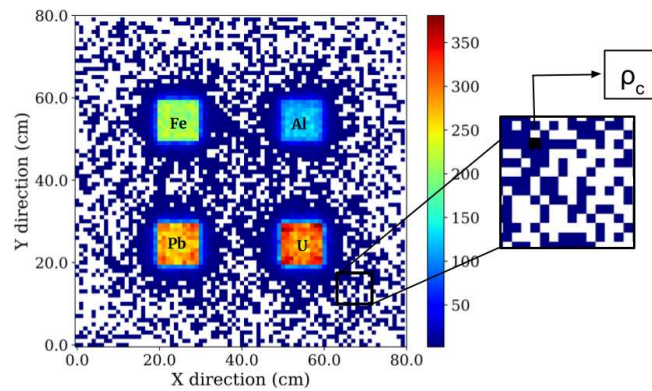


Figure 3. The figure showing the XY projection of scattering vertices (S-map) demonstrates the image analysis technique. Each pixel is attributed the analysis parameter: scattering vertex density (ρ_c). The magnified section of the S-map displays the parameter (ρ_c) of the highlighted pixel.

5. Analysis

This section discusses the background noise reduction achieved using PRM and material identification by implementing a SVM classifier.

5.1. Noise Reduction by Pattern Recognition Method

The reduction in background noise from the image plays an important role in identifying the positions of different blocks. Apart from track selection criteria, background noise has been further minimized using PRM [24]. It is a filtering algorithm wherein a specific pattern of a reference image is used to design a filter “K” called kernel. This K is then used to scan the test image to look for similar properties. It performs like a high-pass filter that allows the range of values lying above a certain threshold due to prior training. We have used PRM to eliminate the noisy events in the 2D S-map shown in Figure 3. The ρ_c obtained for the Al block has been used as the threshold to train the kernel. Since it increases with Z of the material, ρ_c for Al has been kept as the lowest threshold to minimise the noise in the 2D image. Figure 4 illustrates the result of applying the PRM to the image obtained in Section 4.2.

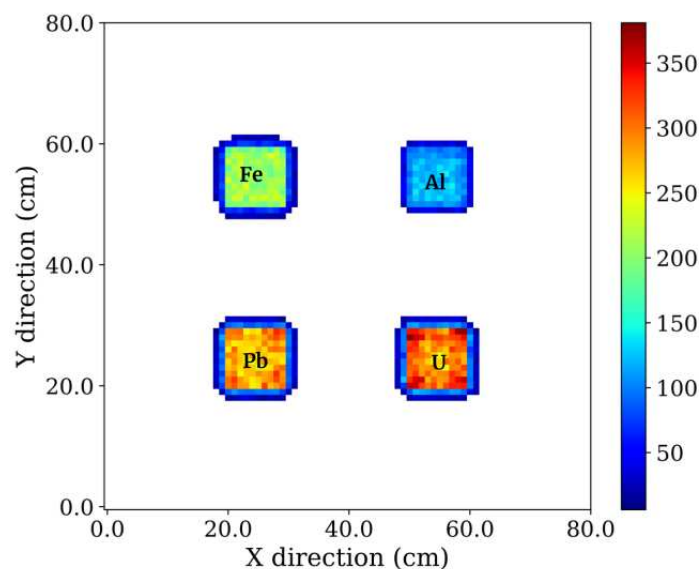


Figure 4. S-maps of scattering vertices after applying PRM.

5.2. Machine Learning for Material Identification

The ML technique used in this project is mainly confined to supervised learning, wherein the computer model based on SVM is trained with manually labelled data. Once trained, it is then used to classify the data according to the trained labels. SVM is a supervised learning method with associated learning algorithms that analyse data for classification. It is one of the most robust classification methods, and is well-known for its simple implementation and fast computation [25]. What sets SVM apart from other classification algorithms, such as Naive Bayes, decision tree, and logistic regression is that it draws a hyperplane instead of a hard-margin to segregate two classes, as shown in Figure 5. It optimizes the decision boundary by finding closest points to the margins and maximizing their distance from the line. This contributes to the generalization of the model and makes it robust to a wide range of outliers in different sample spaces used for analysis. To deal with non-linear data points, as in case of distinction between Pb and U, SVM makes use of the kernel in which the data points are mapped into high-dimensional feature space, thus converting it into a linear classification model. We have employed the polynomial kernel to distinguish between the two materials.

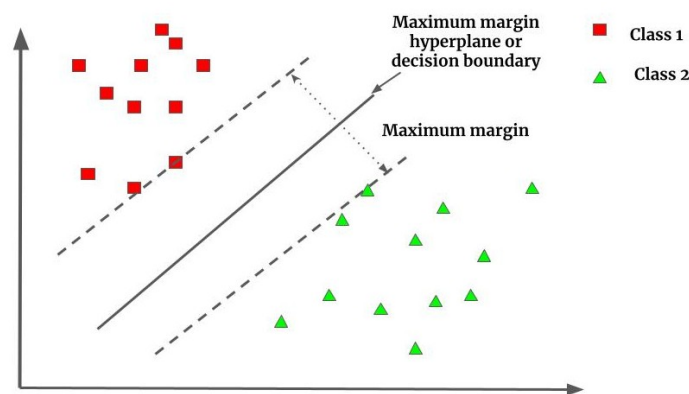


Figure 5. Working principle of an SVM classifier algorithm. The two classes are represented by green triangles and red squares. A decision boundary separating the two classes is defined and optimized by maximizing the distance between extreme vector points.

5.3. Training the SVM Classifier

The SVM classifier has been trained on around 100 datasets each corresponding to 24 h of muon exposure. The parameters ρ_c and θ_{avg} , derived from each pixel of the respective region of blocks, have been passed to the One-Vs-One classifier [30], labeling them as Al: 1, Fe: 2, Pb: 3, and U: 4. The dataset has been split into training and testing sets of 75% and 25%, respectively. During training and testing, ρ_c has been scaled per minute in order to bring all the points corresponding to different exposure rates, i.e., 1, 5, and 24 h in the same range for better visual comparison. The plots of ρ_c versus θ_{avg} for each material (Al, Fe, Pb, and U) are illustrated in Figure 6 for different exposure rates. It has been observed that in case of high-Z materials Pb and U, classification becomes difficult and there is a significant overlapping of ρ_c for these two materials. However, θ_{avg} for U is still higher than Pb. Therefore, training the classifier using both the parameters brings out a better distinction and can be used for material identification as well. To quantify the performance of the trained SVM classifier, we have calculated the binary misclassification rate (R_m) for each of the materials. It has been observed that for longer exposure hours, i.e., 5 and 24 h, the model has been easily able to classify between low and mid-Z materials. The value of R_m for each combination of material has been given in Table 1.

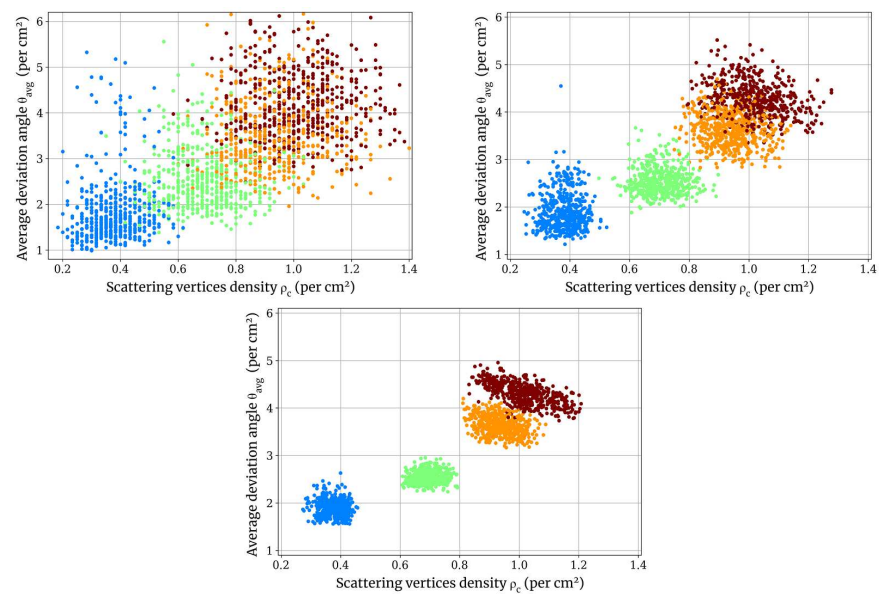


Figure 6. ρ_c (per minute) vs. θ_{avg} (degree) plot for 1 h, 5 h, and 24 h data.

Table 1. Misclassification rate (R_m) for different combination of material blocks.

Exposure Time (h)	Al-Fe	Fe-Pb	Pb-U
1	4.5	7.3	25.7
5	0.0	0.3	1.9
24	0.0	0.0	0.5

6. Inspection of the Rusted Rebar

The ML model with ρ_c and θ_{avg} as the training parameters has been further applied to analyse the defects in civil structure. We have chosen a typical defect commonly found in concrete structures, i.e., rusting of the steel bar in the RCC structures [14,16,21].

6.1. Simulation Setup

A concrete block with rusted steel rebar embedded at its centre has been modeled in Geant4. The rebar is placed in the middle of the RoI with its central axis lying along the X-axis. Fe_2O_3 composition has been used as rust with density 5.25 gm/cc, while steel and concrete have been simulated with density 7.87 gm/cc and 2.3 gm/cc, respectively. Figure 7 shows the inspection setup for RCC with multiple corroded regions. Two variations of rust percentage (15% and 30% of the cross section of the rebar) have been used for the current work (see Table 2 for more details). In the simulation geometry, the pair of detector layers has been placed at a distance of 50 cm while individual detectors have been separated by 7 cm. To ensure hit uniformity, the XY dimension of the detectors has been chosen as 60 cm \times 60 cm and a spatial resolution of 200 μ m has been assumed.

Table 2. Specifications of the rusted rebar for different cases.

Rust Type	Rebar Diameter (mm)	Rust Thickness (mm)
Without rust	30.0	0.0
15% rust	25.5	2.25
30% rust	21.0	4.5

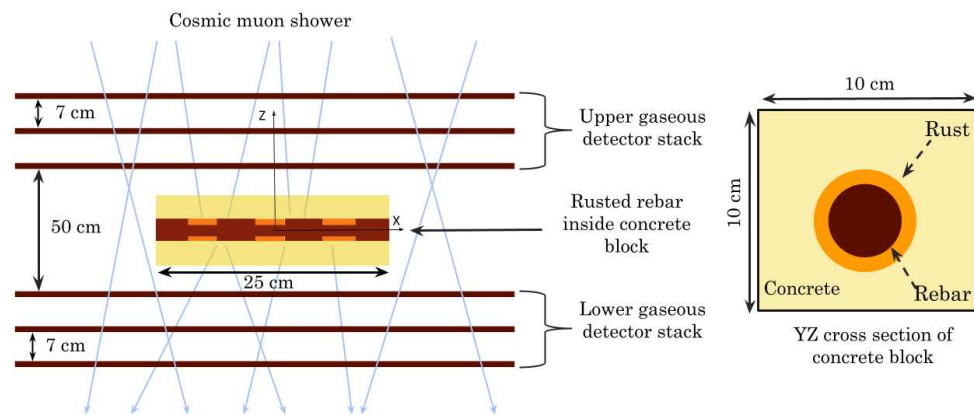


Figure 7. Simulation setup for a rusted rebar. The rusted region (orange) of the steel rebar (brown) is enclosed within the concrete block (yellow).

6.2. Analysis

Following the methods discussed in the above sections, the defective rebar has been analysed for quality assessment. The ROI has been divided into 160×80 pixels of area $2.5 \text{ mm} \times 2.5 \text{ mm}$. For each pixel, scattering vertex and deviation angle have been calculated for constructing projected S-maps. Next, PRM is applied to remove the background noise. The noise minimised images for different cases (perfect, 15% and 30% rust) have been shown in Figure 8. We used SVM classifier to inspect the rebar health with respect to a perfect (without rust) target. The classifier has been trained using two parameters, i.e., scattering vertex density (ρ_c) and average deviation angle (θ_{avg}) extracted from the perfect rebar. The trained model is further used to test the different test cases (perfect, 15% and 30% rusted region) for three different muon exposure. The rebar pixels which were identified as concrete and vice versa are calculated as the Misclassification Rate (R_m). From Figure 8, we can assume that the rusted portion of the rebar will be identified as concrete. Hence, R_m for perfect rebar is considered as the training error and for other cases, it signifies as the measure of rust present in the defective rebar. Therefore, a 7.3% R_m for the 30% rust test case indicates that amount of rust present in this case is greater than the perfect and 15% rusted test case wherein R_m corresponds to 1.1% and 1.4%, respectively. The R_m values for different exposure have been shown in Table 3.

Table 3. Misclassification rate (R_m) for different percentage of rust.

Exposure Time (Days)	Without Rust	15% Rust	30% Rust
3	22.3	23.0	27.8
15	4.5	10.9	14.7
30	1.1	1.4	7.3

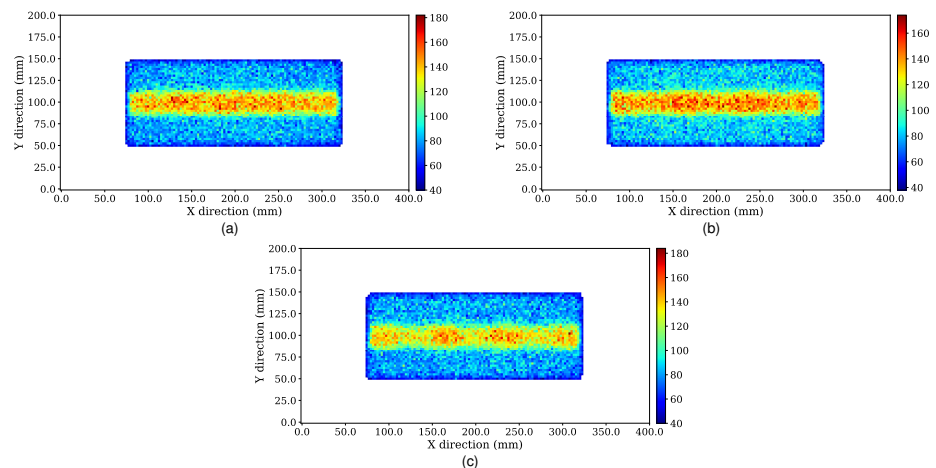


Figure 8. Scattering vertices density (ρ_c) plots for (a) Whole rod without rust, (b) 15% rust, and (c) 30% rust. PRM has been used to eliminate the noisy background. The concrete mixture has been clearly distinguished from the steel rod in all three images. The rusted part has been shown to be distinguished from steel rod in (b,c). The increasing defects involving the rusted parts are reflected in the reconstructed images too.

7. Conclusions

MST as an NDE to image rusted rebars has been investigated based on a numerical simulation. This article also emphasizes the use of a pattern recognition technique for high-quality discrimination of the concrete structure from the background for a lesser cosmic muon exposure. Furthermore, the produced radiographs have been analyzed using an SVM classifier not only for better defect recognition but also to estimate the degradation status. The classifier has been trained and validated using a simple configuration of blocks of pure materials before being used for the identification of contrast in a complex structure, namely RCC. The images obtained for defective cases have been compared to the perfect case and the efficacy of identification has been expressed in terms of misclassification rate (R_m). The present MST system has been found to be able to discriminate between low-Z and mid-Z materials, with 100% accuracy for a nominal exposure (24 h). In the same manner, for rebars with 15% and 30% thickness rusted, the (R_m) has been found to be increasing for a higher percentage of rust with the increased exposure. On the whole, the authors conclude that using the SVM classification model on MST data with nominal exposure (30 days) can be used to identify critical defects in civil structures. In spite of the natural smearing of muons, low radiation rate, and vast momentum distribution, muography can be a potential NDE candidate for monitoring degrading concrete infrastructure. Moreover, environmental parameters, detector efficiencies, resolutions, and setup orientation are several criteria that can impact the imaging. Although, unlike other imaging techniques, muography requires a longer duration of exposure, it has several suitabilities, such as availability of source at no cost, high penetration power, and non-hazardous nature.

Author Contributions: Conceptualization, S.D., S.T. and N.M.; methodology, S.D., S.T. and P.J.; software, S.D., S.T. and P.J.; validation, S.D., S.T., P.B., N.M. and S.M.; formal analysis, S.D. and S.T.; investigation, S.D., S.T., P.J., P.B., N.M. and S.M.; resources, N.M. and S.M.; data curation, S.D., P.J. and S.T.; writing—original draft preparation, S.D. and P.J.; writing—review and editing, S.T., P.B., N.M. and S.M.; visualization, S.D., S.T., P.J., P.B., N.M. and S.M.; supervision, N.M.; project administration, N.M. and S.M.; funding acquisition, N.M. and S.M. All authors have read and agreed to the published version of the manuscript.

Funding: This research was funded by Department of Atomic Energy, University Grants Commission and Government of India.

Institutional Review Board Statement: Not applicable.

Informed Consent Statement: Not applicable.

Data Availability Statement: Not applicable.

Conflicts of Interest: The authors declare no conflict of interest.

References

1. Mattock, A.H.; Chen, K.; Soongswang, K. The behavior of reinforced concrete corbels. *PCI J.* **1976**, *21*, 52–77. [CrossRef]
2. Shubin, A.A.; Tulin, P.K.; Potseshkovskaya, I.V. Research of the effect of the concrete reinforcement structure on the stress-strain state of structures. *Int. J. Appl. Eng. Res.* **2017**, *12*, 1742–1751.
3. McGurn, J. Stainless steel reinforcing bars in concrete. In Proceedings of the International Conference of Corrosion and Rehabilitation of Reinforced Concrete Structures, Orlando, FL, USA, 8–11 December 1998, FHWA: Orlando, FL, USA, 1998.
4. Dong, W.; Wu, Z.; Zhou, X.; Tan, Y. Experimental studies on void detection in concrete-filled steel tubes using ultrasound. *Constr. Build. Mater.* **2016**, *128*, 154–162. [CrossRef]
5. Abdel-Qader, I.; Yohali, S.; Abudayyeh, O.; Yehia, S. Segmentation of thermal images for non-destructive evaluation of bridge decks. *Ndt E Int.* **2008**, *41*, 395–405. [CrossRef]
6. Maierhofer, C.; Röellig, M.; Schlichting, J. Active thermography for evaluation of reinforced concrete structures. In *Non-Destructive Evaluation of Reinforced Concrete Structures*; Elsevier: Amsterdam, The Netherlands, 2010; pp. 370–402.
7. Bungey, J. Sub-surface radar testing of concrete: A review. *Constr. Build. Mater.* **2004**, *18*, 1–8. [CrossRef]
8. Sansalone, M.J.; Streett, W.B. Impact-Echo. *Nondestructive Evaluation of Concrete and Masonry*. The Book: Bullbrier Press, PA, United States, 1997. Available online: <http://impact-echo.com/book/> (accessed on 30 September 2022).
9. George, E.P. Cosmic rays measure overburden of tunnel. *Commonw. Eng.* **1955**, 455.
10. Alvarez, L.W.; Anderson, J.A.; Bedwei, F.E.; Burkhard, J.; Fakhry, A.; Girgis, A.; Goneid, A.; Hassan, F.; Iverson, D.; Lynch, G.; et al. Search for Hidden Chambers in the Pyramids: The structure of the Second Pyramid of Giza is determined by cosmic-ray absorption. *Science* **1970**, *167*, 832–839. [CrossRef]
11. Nagamine, K. Geo-tomographic observation of inner-structure of volcano with cosmic-ray muons. *J. Geogr. Chigaku Zasshi* **1995**, *104*, 998–1007. [CrossRef]
12. Saracino, G.; Amato, L.; Ambrosino, F.; Antonucci, G.; Bonechi, L.; Cimmino, L.; Consiglio, L.; Alessandro, R.; Luzio, E.D.; Minin, G.; et al. Imaging of underground cavities with cosmic-ray muons from observations at Mt. Echia (Naples). *Sci. Rep.* **2017**, *7*, 1181. [CrossRef]
13. Yang, G.; Ireland, D.; Kaiser, R.; Mahon, D. Machine Learning for Muon Imaging. In *Proceedings of the International Conference on Brain Inspired Cognitive Systems*; Springer: Berlin/Heidelberg, Germany, 2018; pp. 808–817.
14. Dobrowolska, M.; Velthuis, J.; Kopp, A.; Perry, M.; Pearson, P. Towards an application of muon scattering tomography as a technique for detecting rebars in concrete. *Smart Mater. Struct.* **2020**, *29*, 055015. [CrossRef]
15. Niederleithinger, E.; Gardner, S.; Kind, T.; Kaiser, R.; Grunwald, M.; Yang, G.; Redmer, B.; Waske, A.; Mielentz, F.; Effner, U.; et al. Muon Tomography of the Interior of a Reinforced Concrete Block: First Experimental Proof of Concept. *J. Nondestruct. Eval.* **2021**, *40*, 1–14. [CrossRef]
16. Tripathy, S.; Datta, J.; Majumdar, N.; Mukhopadhyay, S. Numerical evaluation of a muon tomography system for imaging defects in concrete structures. *Eur. Phys. J. Plus* **2021**, *136*, 824. [CrossRef]
17. Schultz, L.J.; Borozdin, K.N.; Gomez, J.J.; Hogan, G.E.; McGill, J.A.; Morris, C.L.; Priedhorsky, W.C.; Saunders, A.; Teasdale, M.E. Image reconstruction and material Z discrimination via cosmic ray muon radiography. *Nucl. Instrum. Meth. A* **2004**, *519*, 687–694. [CrossRef]
18. Clarkson, A.; Hamilton, D.J.; Hoek, M.; Ireland, D.G.; Johnstone, J.; Kaiser, R.; Keri, T.; Lumsden, S.; Mahon, D.F.; McKinnon, B.; et al. The design and performance of a scintillating-fibre tracker for the cosmic-ray muon tomography of legacy nuclear waste containers. *Nucl. Instrum. Methods Phys. Res. Sect. Accel. Spectr. Detect. Assoc. Equip.* **2014**, *745*, 138–149. [CrossRef]
19. Jonkmans, G.; Anghel, V.; Jewett, C.; Thompson, M. Nuclear waste imaging and spent fuel verification by muon tomography. *Ann. Nucl. Energy* **2013**, *53*, 267–273. [CrossRef]
20. Martínez Ruiz del Arbol, P.; Gomez Garcia, P.; Diez Gonzalez, C.; Oriol Alonso, A. Non-destructive testing of industrial equipment using muon radiography. *Philos. Trans. R. Soc.* **2019**, *377*, 20180054. [CrossRef] [PubMed]
21. Dobrowolska, M.; Velthuis, J.; Kopp, A.; De Sio, C.; Milne, R.; Pearson, P. Development of muon scattering tomography for a detection of reinforcement in concrete. *Eng. Res. Express* **2021**, *3*, 035037. [CrossRef]
22. Highland, V.L. Some Practical Remarks on Multiple Scattering. *Nucl. Instrum. Meth.* **1975**, *129*, 497. [CrossRef]
23. Allison, J.; Amako, K.; Apostolakis, J.; Araujo, H.; Arce Dubois, P.; Asai, M.; Barrand, G.; Capra, R.; Chauvie, S.; Chytracsek, R.; et al. Geant4 developments and applications. *IEEE Trans. Nucl. Sci.* **2006**, *53*, 270–278. [CrossRef]
24. Tripathy, S.; Datta, J.; Majumdar, N.; Mukhopadhyay, S. Material Discrimination in Cosmic Muon Imaging using Pattern Recognition Method. *JINST* **2020**, *15*, P06029. [CrossRef]
25. Support Vectpr Machines. Available online: <https://scikit-learn.org/stable/modules/svm.html> (accessed on 30 September 2022).
26. Cosmic Rays. Available online: <https://pdg.lbl.gov/2020/reviews/rpp2020-rev-cosmic-rays.pdf> (accessed on 30 September 2022).
27. Moliere, G. Theory of scattering of fast charged particles ii multiple and multiple scattering. *J. Nat. Res.* **1948**, *3*, 78–97.

-
28. Lynch, G.R.; Dahl, O.I. Approximations to multiple Coulomb scattering. *Nucl. Instrum. Methods Phys. Res. Sect. Beam Interact. Mater. Atoms* **1991**, *58*, 6–10. [[CrossRef](#)]
 29. Hagemann, C.; Lange, D.; Wright, D. Cosmic-ray shower generator (CRY) for Monte Carlo transport codes. In Proceedings of the 2007 IEEE Nuclear Science Symposium Conference Record, Honolulu, HI, USA, 26 October–3 November 2007; Volume 2, pp. 1143–1146.
 30. One-Vs-One Classifier. Available online: <https://scikit-learn.org/stable/modules/generated/sklearn.multiclass.OneVsOneClassifier.html> (accessed on 30 September 2022).